

Realisation of versatile and effective quantum metrology using a single bosonic mode

Xiaozhou Pan,^{1,*} Tanjung Krisnanda,^{1,†} Andrea Duina,¹ Kimin Park,² Pengtao Song,¹
Clara Yun Fontaine,¹ Adrian Copetudo,¹ Radim Filip,² and Yvonne Y. Gao^{1,3,‡}

¹*Centre for Quantum Technologies, National University of Singapore, Singapore 117543, Singapore*

²*Department of Optics, Palacky University, 77146 Olomouc, Czech Republic*

³*Department of Physics, National University of Singapore, Singapore 117542, Singapore*

(Dated: March 25, 2024)

Quantum metrology offers superior measurement precision compared to classical counterparts. Traditionally, achieving this enhancement involves employing multi-particle entangled quantum states, necessitating state preparation and detection schemes that are practically challenging. In this article, we present a versatile and on-demand protocol for deterministic parameter estimation that leverages two state-transfer operations on a single bosonic mode. Specifically, we demonstrate this protocol in the context of phase and amplitude estimation using the superposition of coherent states in the bosonic circuit quantum electrodynamics (cQED) platform. With low photon numbers of up to 1.76, we achieve quantum-enhanced precision approaching the Heisenberg scaling, reaching a metrological gain of 7.5(6) dB and 9.3(5) dB respectively for phase and amplitude estimation. We show that the gain or sensitivity range can be further enhanced on the fly by tailoring the input states based on specific system constraints. Our protocol can be adapted to further optimize the desired figures of merit using tailored quantum states or operations, not only for bosonic cQED hardware but also readily extensible to other continuous-variable platforms. The realisation of this versatile and effective scheme affords a promising path towards practical quantum-enhanced sensing.

Quantum metrology utilizes optimally chosen sets of quantum states and measurement schemes to attain measurement precision beyond what is possible with classical states [1]. This quantum-enhanced precision appeals to many disciplines. For example, it has already applications for sensing magnetic fields [2, 3], electric fields [4, 5], and displacements [5, 6], as well as improving clock stability [7, 8] and quantum imaging [9, 10]. It is also expected to enhance gravitational wave detection in LIGO [11, 12] and the search for dark matter [13].

One of the earliest and most canonical examples is quantum-enhanced phase estimation in a two-mode interferometer [14, 15]. The use of coherent states (CS) defines the standard quantum limit (SQL) with precision $\Delta\theta = 1/\sqrt{N}$, where $\Delta\theta$ is the standard deviation of the phase and N is the number of particles or excitations. Using entanglement as the resource state in this configuration, the precision scales as $\Delta\theta = 1/N$ (known as the Heisenberg limit), which affords a \sqrt{N} improvement over the SQL. This enhanced precision has been demonstrated in many experiments using entangled multipartite systems [16–20]. Practically, however, both the preparation of these non-local states and the implementation of correlated or conditional measurements can be challenging. Furthermore, preparing such quantum states often demands post-selection or heralding, which undermines the quantum enhancement [21, 22] over deterministically created coherent states.

In light of these challenges, there has been growing interest in quantum metrology using non-entangled states [23]. For instance, Fock states are used to perform phase-insensitive measurements with enhanced precision due to their nonclassical features [24, 25]. Quantum-enhanced phase estimation has also been shown using displaced Fock states or their superposition [26–28]. This handily bypasses the demanding non-local operations, which generally suppress the quantum advantage under even slight decoherence. However, the existing single-mode schemes are system-specific, as they rely on highly-specialised input states or quantum gates.

Here, we demonstrate a versatile and on-demand protocol for deterministic parameter estimation using a single bosonic mode. With standard bosonic cQED hardware, we show quantum-enhanced performance for both phase and amplitude estimation, achieving state-of-the-

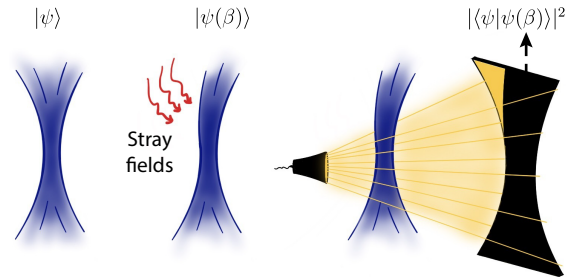


FIG. 1. **Universal quantum metrology with a single bosonic mode.** The approach consists of three fundamental steps: preparation of input state $|\psi\rangle$; distortion from the to-be-estimated process, potentially induced by stray fields, which effectively encode the parameter of interest β into the state $|\psi(\beta)\rangle$; and information retrieval by projection onto the initial state, depicted by the shaded region.

* Contributed equally to this article.

Corresponding author: xiaozhou@nus.edu.sg

† Contributed equally to this article.

Corresponding author: tanjung@nus.edu.sg

‡ Corresponding author: yvonne.gao@nus.edu.sg

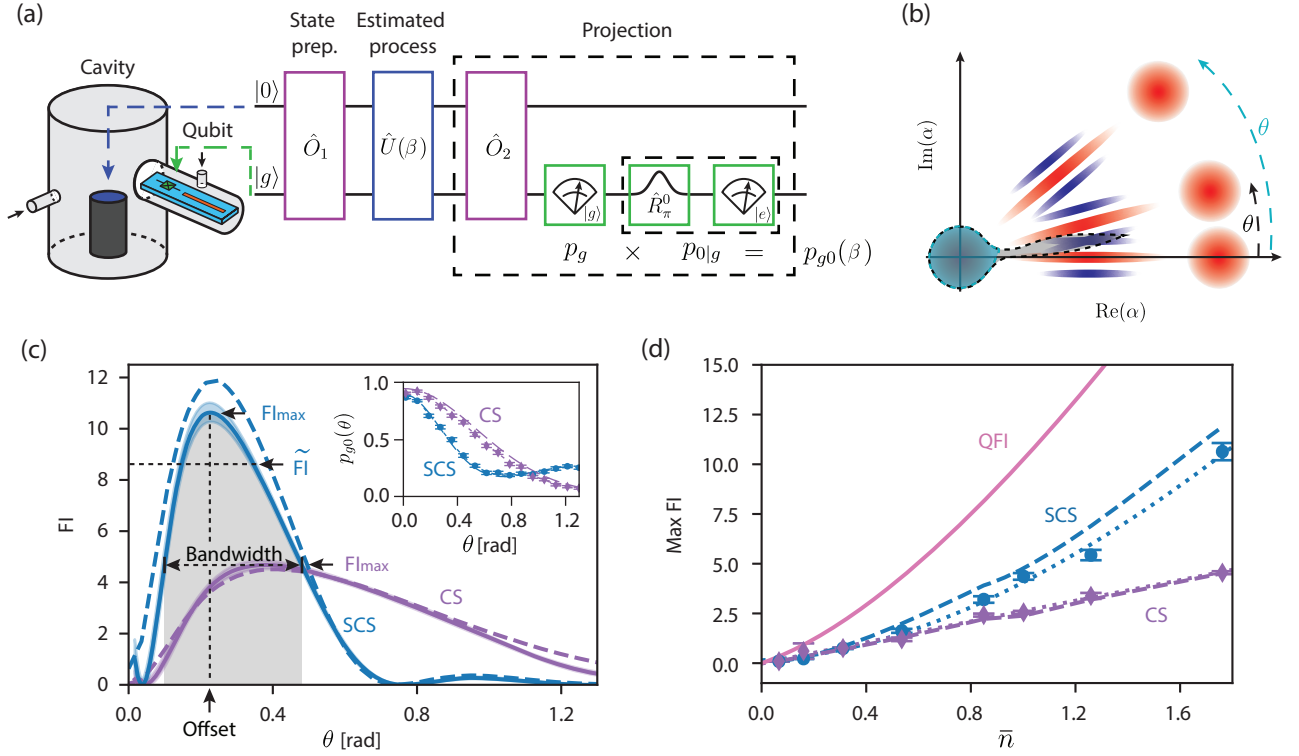


FIG. 2. **Parameter estimation procedure with bosonic cQED.** (a) Implementation of the protocol in cQED. A cavity stores a bosonic mode, coupled to a transmon qubit. The readout resonator provides single-shot measurements of the qubit state. The protocol includes a state-transfer operation \hat{O}_1 , a process $\hat{U}(\beta)$, and a projection operation involving a state-transfer operation \hat{O}_2 , qubit measurement p_g , and cavity measurement $p_{0|g}$. (b) Illustration of phase estimation using SCS. The shaded area visualises the overlap between the distorted and initial state $|\langle\psi|\psi(\theta)\rangle|^2$. (c) The FI for SCS (solid blue) and CS (solid purple), calculated using Eq. (1), where p is from the polynomial fit (dotted curves) of the experimental $p_{g0}(\theta)$ (markers) in the inset. The shaded area with the corresponding color indicates the standard deviation error from bootstrapping. Bandwidth is defined as the range on which the FI of SCS is above the maximum FI (FI_{\max}) of CS. The grey area represents the region where we have a quantum advantage compared to CS and \bar{FI} is its corresponding average FI. Dashed curves show simulation. (d) The FI_{\max} for SCS (blue) and CS (purple) are plotted as markers for states with different photon numbers \bar{n} . The errors are standard deviation from bootstrapping. Dashed curves are simulation and dotted curves are fitting: $3.92(9)\bar{n}^{-1.71(1)} + 0.15(4)$ for SCS and $2.62(6)\bar{n}^{-0.99(1)} + 0.00(4)$ for CS. The solid pink curve is the ideal QFI of SCS.

art metrological gain in the low photon number regime. We present a comprehensive analysis of key metrological figures of merit, including the sensitivity bandwidth, average sensitivity within the bandwidth, and adjustment of the position of maximum sensitivity. Importantly, we show that our implementation allows these key figures to be optimally traded on the fly to best suit the intended metrological goal by simply varying a few programmable pulse parameters in the protocol. Our strategy is universal across different physical systems and can be applied to other physical implementations of bosonic modes, such as optical resonators [29], trapped ions [30], neutral atoms [31], and mechanical resonators [32].

Conceptually, our methodology is akin to shining lights on an object under the influence of some external perturbations and comparing the resulting shadow with the original unperturbed object, as illustrated in Fig. 1(a). The shadow represents the projection of the distorted state $|\psi(\beta)\rangle = \hat{U}(\beta)|\psi\rangle$, writ-

ten as $p(\beta) = |\langle\psi|\psi(\beta)\rangle|^2$ where β is the to-be-estimated parameter, $\hat{U}(\beta) = \exp(i\hat{B}\beta)$, and we shall refer to \hat{B} as the *process generator*. The measurement outcome $p(\beta)$ provides an optimal precision for estimating β [33], as indicated by the Fisher information (FI)

$$F(\beta) = \frac{1}{p(\beta)(1-p(\beta))} \left(\frac{\partial p(\beta)}{\partial \beta} \right)^2, \quad (1)$$

which provides a lower asymptotic bound on the achievable precision, i.e., $\Delta\beta \geq 1/\sqrt{F}$, known as the Cramér-Rao bound [34]. The optimality transpires as the FI saturates its maximum value given by the quantum Fisher information (QFI) $F_q = 4(\Delta\hat{B})^2$, where $(\Delta\hat{B})^2 = \langle\psi|\hat{B}^2|\psi\rangle - \langle\psi|\hat{B}|\psi\rangle^2$. In addition to having an optimal measurement scheme, it is also important to choose the input states strategically for optimal metrological performance, i.e., those with high variance $(\Delta\hat{B})^2$.

We implement this generalised metrology scheme on standard cQED hardware as depicted in Fig. 2(a). Ini-

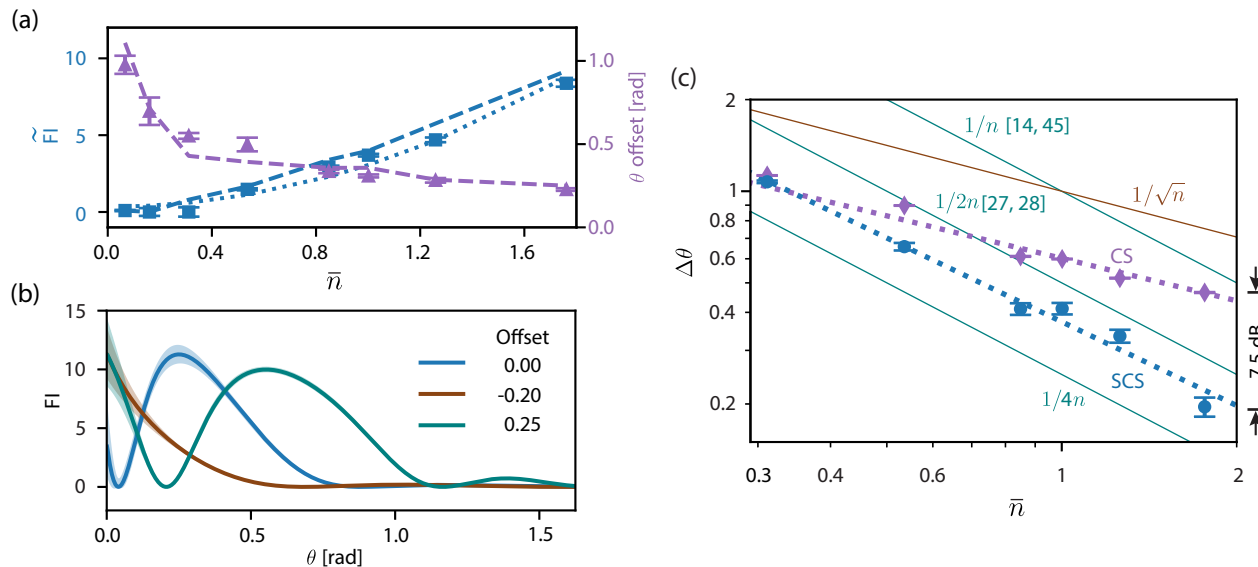


FIG. 3. **Comprehensive analysis for phase estimation and quantum-enhanced precision.** (a) The average FI (\bar{F}) of SCS within the bandwidth and θ offset at which FI is maximum vs \bar{n} . The dotted curve is a fit: $2.7(3)\bar{n}^{2.0(1)} + 0.3(1)$. (b) The same protocol as in Fig. 2(c) with initial states prepared with offset in θ . As the protocol is symmetrical with respect to θ , maximum FI at $\theta = 0$ can be obtained by a positive/negative offset of about 0.2 – 0.25 rad. (c) The phase precision vs \bar{n} for both SCS (blue circles) and CS (purple diamonds). The solid lines are different theoretical Heisenberg limits and SQL. The dotted lines are linear fit: $\log(\Delta\theta) = -0.915(2)\log(\bar{n}) - 0.987(1)$ for SCS and $\log(\Delta\theta) = -0.464(1)\log(\bar{n}) - 0.508(1)$ for CS. The highest metrological gain for SCS compared to CS with the same photon number is 7.5(6) dB.

tially, a desired quantum state is prepared with a state-transfer unitary \hat{O}_1 , i.e., $|g\psi\rangle = \hat{O}_1|g0\rangle$. After the system undergoes a process $\hat{U}(\beta)$, a projection measurement is performed with a unitary \hat{O}_2 and qubit-cavity measurements. The operation \hat{O}_2 can be done with *any* state-transfer unitary such that $|g0\rangle = \hat{O}_2|g\psi\rangle$. Finally, standard measurements are performed to obtain the probabilities of the qubit in the ground state p_g and cavity in vacuum $p_{0|g}$, which is achieved by driving the qubit with a vacuum-selective π -pulse and measuring the qubit in the excited state. The projection yields the probability $p_{g0} = |\langle\psi|\hat{U}(\beta)|\psi\rangle|^2$ [33]. An important advantage of our protocol is that any two operations \hat{O}_1 and \hat{O}_2 realising the required state transfers are sufficient. This minimalistic approach makes it highly adaptable to a variety of hardware parameters and readily extensible to different physical systems with their preferred native gates. For instance, in cQED platforms featuring small qubit-oscillator dispersive coupling, $\hat{O}_{1,2}$ can be realised using echoed conditional displacement (ECD) gates [35, 36]; whereas devices with more significant dispersive coupling can leverage on gradient ascent pulse engineering (GRAPE) [37–39] or selective number-dependent arbitrary phase gates [40]. Beyond cQED, the state transfer operations can be achieved through coherent coupling of the internal-motional states of trapped ions/atoms [27, 41], ECD gates in an atom-light system in cavity-QED [42], or swap gates in qubit-mechanical resonator system in quantum acoustics [43].

We first demonstrate this universal protocol in the con-

text of phase estimation in cQED. The target process is enacted via the dispersive qubit-cavity coupling with Hamiltonian $H_{\text{int}}/\hbar = (\chi/2)\hat{\sigma}_z\hat{a}^\dagger\hat{a}$, where χ is the coupling strength, $\hat{\sigma}_z$ the z -Pauli matrix, and $\hat{a}(\hat{a}^\dagger)$ is the annihilation (creation) operator of the bosonic cavity. For a qubit in the ground state $|g\rangle$, the dynamics realises a unitary for the cavity $\hat{U}(\theta) = \exp(i\hat{a}^\dagger\hat{a}\theta)$, with $\theta = \chi t/2$. As a result, the process generator is given by $\hat{n} = \hat{a}^\dagger\hat{a}$, which means useful states here are those with high variance in photon number $(\Delta\hat{n})^2$.

Theoretically, we investigate states with high photon number variances such as (listed from lowest to highest) superposition of Fock states, superposition of coherent states (SCS), and squeezed vacuum. Experimentally, we find SCS to be the most robust against device imperfections such as self-Kerr and offer the highest sensitivity in our system [33]. Therefore, we shall primarily focus on SCS, given by $\mathcal{N}_\alpha(|0\rangle + |\alpha\rangle)$ (in short SCS(α)), with the normalisation factor \mathcal{N}_α , to demonstrate the efficacy of our strategy. The intuition behind the performance of SCS for phase estimation is understood by visualizing the projection $p_{g0} = |\langle\psi|\hat{U}(\theta)|\psi\rangle|^2$ in phase space, see Fig. 2(b). With this illustration in mind, we note two important observations. Firstly, as θ increases, the probability $p_{g0}(\theta)$ changes from 1 to a constant value, where the fringes do not overlap and the probability is insensitive to a further increase in θ . Secondly, the use of higher α (further right position of the right blob in Fig. 2(b)) will reduce the overlap more sharply at lower θ , making the detection more sensitive to θ at the cost of a smaller

range of sensitivity.

Experimentally, we chose to implement the state transfer operations $\hat{O}_{1,2}$ using GRAPE, which is a convenient and widely used tool in cQED [28, 37–39]. However, this choice is not unique, e.g., in the weak dispersive regime, one may opt to use ECD gates to create SCS [44]. By executing the gate sequence in Fig. 2(a), we directly obtain the probability $p_{g0}(\theta)$. An exemplary plot comparing the use of SCS ($\alpha = 2$) and CS with the same average photon number $\bar{n} = \langle \hat{a}^\dagger \hat{a} \rangle$, is presented in Fig. 2(c) inset. Each single-shot measurement is one bit of information and we perform 1000 repetitions for each point to obtain the statistics. The experimental data shows good agreement with simulations (corresponding dashed curves), which take into account decoherences and measurement imperfections [33]. It is apparent from the probability that the SCS is more sensitive to the change in θ than the CS.

To quantitatively examine the performance of our implementation, we compute the FI in Eq. (1), where the corresponding p is a smooth function obtained from the polynomial fit of $p_{g0}(\theta)$. The resulting FI for SCS and CS are plotted in Fig. 2(c) as solid blue and purple curves, respectively. As expected, the maximum FI of SCS beats that of the CS at the cost of the sensitivity range. Furthermore, figure 2(d) shows the maximum FI for SCS (blue circles) and CS (purple diamonds) for states with different photon numbers. We note that decoherence and experimental imperfections hinder our results from reaching the ideal QFI of SCS (pink solid curve), as by simulations (corresponding dashed curves) with real device parameters. However, despite that, second-order polynomial fits (corresponding dotted curves) show that the FI_{max} of SCS is nearly quadratic, whereas that of the CS is linear, which indicates a clear $\sqrt{\bar{n}}$ quantum enhancement in the estimation precision.

To holistically evaluate the performance of a quantum metrology scheme, several other important figures of merit must also be considered in conjunction with the maximum FI. Specifically, these include the parameter range in which we achieve quantum-enhanced precision, the corresponding average sensitivity, and the capability to shift the maximum sensitivity point to origin $\theta = 0$ which is crucial for sensing applications. We define the bandwidth as the range of θ in which the FI of SCS is above the maximum FI of the CS, $\tilde{\text{FI}}$ as the average FI within the bandwidth, and θ offset where the FI is maximum. The bandwidth for SCS up to $\bar{n} = 1.76$ is nearly constant at approximately 0.5 rad, which sets the limit on the allowed phase fluctuations in the system. The $\tilde{\text{FI}}$ against photon number \bar{n} in Fig. 3(a) shows a quadratic trend, suggesting that working within the bandwidth still affords favourable precision scaling. The offset in θ is close to the position of the maximum slope $|\partial p / \partial \theta|$ in the measured probability [33] and decreases for SCS with larger α , as shown in Fig. 3(a). With our versatile protocol, this offset is a fully programmable parameter and can be adjusted by simply preparing input states with an initial phase offset (Fig. 3(b)) to ensure that we can

operate around the maximum sensitivity point.

In addition to the FI, which only sets the lower bound to the precision according to the Cramér-Rao bound, we now present a benchmark for direct calculation of the phase precision, $\Delta\theta$. It is computed as $\Delta\theta = \Delta p / |\partial p / \partial \theta|$, where $\partial p / \partial \theta$ is obtained from the polynomial fit as in Fig. 2(c) inset and Δp is the standard deviation of the single shot measurement with 1000 repetitions. The standard deviation for SCS (blue circles) and CS (purple diamonds) are plotted in Fig. 3(c), which respectively beat the precision limit $\Delta\theta = 1/\bar{n}$ and the SQL ($\Delta\theta = 1/\sqrt{\bar{n}}$) commonly used in optical [14, 15] or atomic [45] interferometers. We also note that the experimentally obtained precision for SCS, $\Delta\theta_{\text{SCS}}$, surpasses the ideal limit used for the superposition of Fock states ($\Delta\theta = 1/2\bar{n}$) [27, 28]. This is because the QFI of SCS and CS in our optimised strategy gives $\Delta\theta = 1/\sqrt{4\bar{n} + 4\bar{n}^2}$ and $\Delta\theta = 1/\sqrt{4\bar{n}}$, respectively [33] to afford superior performance by design. Furthermore, the linear fit of the SCS shows that $\Delta\theta_{\text{SCS}}$ approaches the Heisenberg limit scaling. To benchmark the quantum enhancement of our implementation, we compute the metrological gain of $20 \log_{10}(\Delta\theta_{\text{CS}}/\Delta\theta_{\text{SCS}}) = 7.5(6)$ dB with a low photon number of 1.76. Here, the uncertainty is one standard deviation obtained from bootstrapping and stabilises at ~ 600 measurement repetitions [33].

Moreover, the gain or bandwidth can be enhanced on demand by optimizing the initial states with respect to system constraints. In typical hardware implementations, a device may allow access to a limited maximum photon number \bar{n} or SCS amplitude α , which may be due to photon loss, self-Kerr effect, etc. Depending on the specific hardware limitations and the figures of merit, we can optimise the metrological performance by simply varying the superposition weights of the SCS. Physically, this is achieved by adjusting the qubit and cavity drives for $\hat{O}_{1,2}$, without any changes to the device or system dynamics. For the case where the constraint is the photon number, e.g., $\bar{n} = 1$, we show that higher maximum FI can be achieved by putting more weight on the $|0\rangle$ component of the SCS, at the expense of sensitivity range, as shown in Fig. 4(a). On the other hand, if the constraint is given by the maximum amplitude, e.g., $\alpha = 1.6$, we show states with a higher weight on $|\alpha\rangle$ give a higher maximum FI, without compromising the sensitivity range, see Fig. 4(b). Essentially, in both examples, states with higher photon number variance result in higher maximum FI. We can also make use of the illustration given in Fig. 2(b). If α is fixed, the Wigner function for states with more weight w on the $|\alpha\rangle$ component will have a stronger blob at α . This way the change of probability p_{g0} is from 1 to a number which gets closer to zero with increasing w , resulting in higher sensitivity. However, if \bar{n} is fixed, increasing the weight on the $|\alpha\rangle$ component comes at the cost of using a smaller α , which is a more dominant factor. As a result, the sensitivity is reduced.

To illustrate the versatility of our protocol, we demonstrate quantum-enhanced precision for amplitude estima-

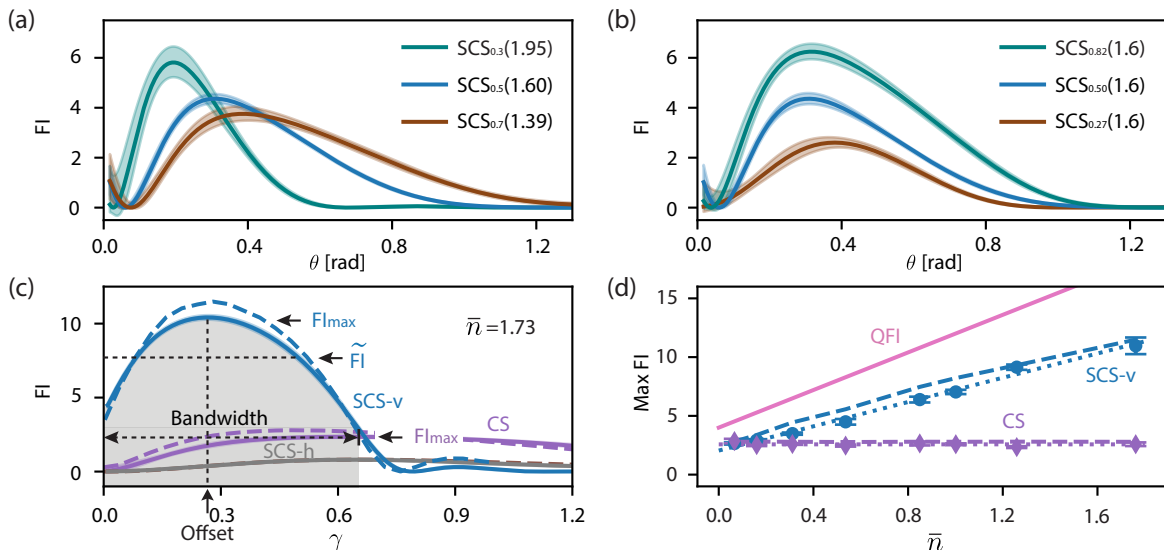


FIG. 4. **On-demand optimization and amplitude estimation.** (a) FI of SCS with different weights and fixed photon number $\bar{n} = 1$. The w in $SCS_w(\alpha)$ denotes the weight in the $|\alpha\rangle$ component, i.e., $\mathcal{N}'(\sqrt{1-w}|0\rangle + \sqrt{w}|\alpha\rangle)$, \mathcal{N}' represents the normalization coefficient. The corresponding shaded area indicates the standard deviation from bootstrapping. (b) Similar to (a) but for SCS with different weights and fixed $\alpha = 1.6$. (c) FI for amplitude estimation using CS (solid purple), SCS-v for amplitude in the vertical direction (solid blue), and SCS-h for amplitude in the horizontal direction (solid grey). The corresponding dashed curves indicate simulation. (d) The maximum FI for SCS-v (blue) and CS (purple) vs photon number \bar{n} . Dashed curves are simulation and dotted curves are fitting: $4.9(2)n^{1.06(2)} + 2.2(1)$ for SCS-v and $0.411(1)n^{0.00(3)} + 2.165(1)$ for CS. The solid pink curve is the ideal QFI of SCS-v.

tion by simply changing the process unitary in Fig. 2(a) to a displacement in the imaginary direction $\hat{U}(\gamma) = \exp(i\gamma(\hat{a}^\dagger + \hat{a}))$, where γ is the displacement amplitude. The process generator is now $\hat{x} = (\hat{a}^\dagger + \hat{a})$, making states with high variance $(\Delta\hat{x})^2$ useful for amplitude estimation. Here, SCS offer high variance $\propto \bar{n}$ compared to CS, which have a constant variance [33]. The illustration is similar to that of phase estimation in Fig. 2(b), except the SCS are now displaced in the imaginary direction instead of rotated. SCS with higher α have more and sharper fringes in between the blobs, such that the overlap with the initial state reduces more sharply as γ increases.

Experimentally, we show that SCS displaced vertically in the imaginary direction (SCS-v) offer the highest FI, compared to both CS and SCS displaced horizontally in the real direction (SCS-h), as shown in Fig. 4(c). This can be explained by noting that SCS-h have a different process unitary $\hat{U}(\gamma) = \exp(i\gamma i(\hat{a} - \hat{a}^\dagger))$, where the process generator is now $\hat{y} = i(\hat{a} - \hat{a}^\dagger)$, such that the variance of SCS is low, even lower than that of the CS.

Furthermore, by operating at the maximum FI, we show that the SCS-v (CS) exhibits a linear (constant) trend against \bar{n} , as shown in Fig. 4(d). This suggests a $\sqrt{\bar{n}}$ quantum-enhanced precision of the SCS-v over the CS. We refer to Ref. [33] for a comprehensive analysis of the FI, which importantly includes the shift of the max FI to the initial position $\gamma = 0$. The $\sqrt{\bar{n}}$ enhancement also manifests in the direct calculation of the amplitude precision, which reveals that $\Delta\gamma \propto 1/\sqrt{\bar{n}}$ for SCS-v and

$\Delta\gamma \approx \text{constant}$ for CS [33]. Finally, directly comparing SCS-v to CS reveals a high metrological gain of 9.3(5) dB.

In summary, we have introduced a versatile and on-demand protocol for parameter estimation using a single bosonic mode. With this scheme, we demonstrated both phase and amplitude estimation using the superposition of coherent states and achieved quantum-enhanced precision $\sim \sqrt{\bar{n}}$ in both cases, compared to classically behaving coherent states. Using states with photon numbers of up to only 1.76, the high variance of SCS results in state-of-the-art metrological gain, 7.5(6) dB for phase and 9.3(5) dB for amplitude estimation. We also demonstrated the on-demand adaption of the scheme to optimise for certain metrological performance metrics with respect to hardware constraints.

The simplicity and effectiveness of our protocol stem from the use of a single bosonic mode with two general state-transfer operations that can be realised by any standard gates. As such, our implementation is accessible to systems with different device parameters. Furthermore, the strategy is universal and can be readily performed with many other bosonic systems beyond cQED using their preferred native operations. Our results demonstrate a simple yet powerful strategy for real metrological applications. For instance, quantities such as stray magnetic, electric field, etc. that may affect the qubit or cavity frequency will result in the change of dispersive coupling strength χ [46], which in turn leads to phase variations on the bosonic state. Hence, the phase precision $\Delta\theta$ obtained in our implementation is directly related

lated to the sensing precision of the relevant physical parameters under investigation. Therefore, our work offers a promising first step towards practical and optimal quantum metrology using a single bosonic system.

Acknowledgement. This project is supported by

the National Research Foundation, Singapore, grant number NRFF12-2020-0063 and NRF2020-NRF-ISF004-3540. RF and KP acknowledge support of 21-13265X of the Czech Science Foundation and EU H2020-WIDESPREAD-2020-5 project NONGAUSS (951737) under the CSA - Coordination and Support Action.

-
- [1] V. Giovannetti, S. Lloyd, and L. Maccone, Quantum-enhanced measurements: beating the standard quantum limit, *Science* **306**, 1330 (2004).
- [2] J. A. Jones, S. D. Karlen, J. Fitzsimons, A. Ardavan, S. C. Benjamin, G. A. D. Briggs, and J. J. Morton, Magnetic field sensing beyond the standard quantum limit using 10-spin noon states, *science* **324**, 1166 (2009).
- [3] M. Napolitano, M. Koschorreck, B. Dubost, N. Behbood, R. Sewell, and M. W. Mitchell, Interaction-based quantum metrology showing scaling beyond the heisenberg limit, *Nature* **471**, 486 (2011).
- [4] A. Facon, E.-K. Dietsche, D. Grosso, S. Haroche, J.-M. Raimond, M. Brune, and S. Gleyzes, A sensitive electrometer based on a rydberg atom in a schrödinger-cat state, *Nature* **535**, 262 (2016).
- [5] K. A. Gilmore, M. Affolter, R. J. Lewis-Swan, D. Barberena, E. Jordan, A. M. Rey, and J. J. Bollinger, Quantum-enhanced sensing of displacements and electric fields with two-dimensional trapped-ion crystals, *Science* **373**, 673 (2021).
- [6] S. Burd, R. Srinivas, J. Bollinger, A. Wilson, D. Wineland, D. Leibfried, D. Slichter, and D. Allcock, Quantum amplification of mechanical oscillator motion, *Science* **364**, 1163 (2019).
- [7] A. D. Ludlow, M. M. Boyd, J. Ye, E. Peik, and P. O. Schmidt, Optical atomic clocks, *Reviews of Modern Physics* **87**, 637 (2015).
- [8] M. F. Riedel, P. Böhi, Y. Li, T. W. Hänsch, A. Sinatra, and P. Treutlein, Atom-chip-based generation of entanglement for quantum metrology, *Nature* **464**, 1170 (2010).
- [9] C. Rouvière, D. Barral, A. Grateau, I. Karuseichyk, G. Sorelli, M. Walschaers, and N. Treps, Ultra-sensitive separation estimation of optical sources, *Optica* **11**, 166 (2024).
- [10] M. Tsang, R. Nair, and X.-M. Lu, Quantum theory of superresolution for two incoherent optical point sources, *Physical Review X* **6**, 031033 (2016).
- [11] M. Tse, H. Yu, N. Kijbunchoo, A. Fernandez-Galiana, P. Dupej, L. Barsotti, C. Blair, D. Brown, S. Dwyer, A. Effler, *et al.*, Quantum-enhanced advanced ligo detectors in the era of gravitational-wave astronomy, *Physical Review Letters* **123**, 231107 (2019).
- [12] H. Yu, L. McCuller, M. Tse, N. Kijbunchoo, L. Barsotti, and N. Mavalvala, Quantum correlations between light and the kilogram-mass mirrors of ligo, *Nature* **583**, 43 (2020).
- [13] K. M. Backes, D. A. Palken, S. A. Kenany, B. M. Brubaker, S. Cahn, A. Droster, G. C. Hilton, S. Ghosh, H. Jackson, S. K. Lamoreaux, *et al.*, A quantum enhanced search for dark matter axions, *Nature* **590**, 238 (2021).
- [14] T. Nagata, R. Okamoto, J. L. O'brien, K. Sasaki, and S. Takeuchi, Beating the standard quantum limit with four-entangled photons, *Science* **316**, 726 (2007).
- [15] S. Shlussarenko, M. M. Weston, H. M. Chrzanowski, L. K. Shalm, V. B. Verma, S. W. Nam, and G. J. Pryde, Unconditional violation of the shot-noise limit in photonic quantum metrology, *Nature Photonics* **11**, 700 (2017).
- [16] X. Guo, C. R. Breum, J. Borregaard, S. Izumi, M. V. Larsen, T. Gehring, M. Christandl, J. S. Neergaard-Nielsen, and U. L. Andersen, Distributed quantum sensing in a continuous-variable entangled network, *Nature Physics* **16**, 281 (2020).
- [17] Z. Li, S. Colombo, C. Shu, G. Velez, S. Pilatowsky-Cameo, R. Schmied, S. Choi, M. Lukin, E. Pedrozo-Peñafiel, and V. Vuletić, Improving metrology with quantum scrambling, *Science* **380**, 1381 (2023).
- [18] C. D. Marciniak, T. Feldker, I. Pogorelov, R. Kaubruegger, D. V. Vasilyev, R. van Bijnen, P. Schindler, P. Zoller, R. Blatt, and T. Monz, Optimal metrology with programmable quantum sensors, *Nature* **603**, 604 (2022).
- [19] T.-W. Mao, Q. Liu, X.-W. Li, J.-H. Cao, F. Chen, W.-X. Xu, M. K. Tey, Y.-X. Huang, and L. You, Quantum-enhanced sensing by echoing spin-nematic squeezing in atomic bose-einstein condensate, *Nature Physics* , 1 (2023).
- [20] J. Franke, S. R. Muleady, R. Kaubruegger, F. Kranzl, R. Blatt, A. M. Rey, M. K. Joshi, and C. F. Roos, Quantum-enhanced sensing on optical transitions through finite-range interactions, *Nature* **621**, 740 (2023).
- [21] K. J. Resch, K. L. Pregnell, R. Prevedel, A. Gilchrist, G. J. Pryde, J. L. O'Brien, and A. G. White, Time-reversal and super-resolving phase measurements, *Physical review letters* **98**, 223601 (2007).
- [22] V. Giovannetti, S. Lloyd, and L. Maccone, Advances in quantum metrology, *Nature Photonics* **5**, 222 (2011).
- [23] D. Braun, G. Adesso, F. Benatti, R. Floreanini, U. Marzolino, M. W. Mitchell, and S. Pirandola, Quantum-enhanced measurements without entanglement, *Reviews of Modern Physics* **90**, 035006 (2018).
- [24] F. Wolf, C. Shi, J. C. Heip, M. Gessner, L. Pezzè, A. Smerzi, M. Schulte, K. Hammerer, and P. O. Schmidt, Motional fock states for quantum-enhanced amplitude and phase measurements with trapped ions, *Nature communications* **10**, 2929 (2019).
- [25] L. Podhora, L. Lachman, T. Pham, A. Lešundák, O. Číp, L. Slodička, and R. Filip, Quantum non-gaussianity of multiphonon states of a single atom, *Physical Review Letters* **129**, 013602 (2022).
- [26] X. Deng, S. Li, Z.-J. Chen, Z. Ni, Y. Cai, J. Mai, L. Zhang, P. Zheng, H. Yu, C.-L. Zou, *et al.*, Heisenberg-limited quantum metrology using 100-photon fock states, *arXiv preprint arXiv:2306.16919* (2023).
- [27] K. C. McCormick, J. Keller, S. C. Burd, D. J. Wineland,

- A. C. Wilson, and D. Leibfried, Quantum-enhanced sensing of a single-ion mechanical oscillator, *Nature* **572**, 86 (2019).
- [28] W. Wang, Y. Wu, Y. Ma, W. Cai, L. Hu, X. Mu, Y. Xu, Z.-J. Chen, H. Wang, Y. Song, *et al.*, Heisenberg-limited single-mode quantum metrology in a superconducting circuit, *Nature communications* **10**, 4382 (2019).
- [29] S. Haroche and J.-M. Raimond, *Exploring the quantum: atoms, cavities, and photons* (Oxford university press, 2006).
- [30] D. Leibfried, R. Blatt, C. Monroe, and D. Wineland, Quantum dynamics of single trapped ions, *Reviews of Modern Physics* **75**, 281 (2003).
- [31] R. Grimm, M. Weidemüller, and Y. B. Ovchinnikov, Optical dipole traps for neutral atoms, in *Advances in atomic, molecular, and optical physics*, Vol. 42 (Elsevier, 2000) pp. 95–170.
- [32] M. Aspelmeyer, T. J. Kippenberg, and F. Marquardt, Cavity optomechanics, *Reviews of Modern Physics* **86**, 1391 (2014).
- [33] See details in supplementary material, .
- [34] S. L. Braunstein and C. M. Caves, Statistical distance and the geometry of quantum states, *Physical Review Letters* **72**, 3439 (1994).
- [35] P. Campagne-Ibarcq, A. Eickbusch, S. Touzard, E. Zalys-Geller, N. E. Frattini, V. V. Sivak, P. Reinhold, S. Puri, S. Shankar, R. J. Schoelkopf, *et al.*, Quantum error correction of a qubit encoded in grid states of an oscillator, *Nature* **584**, 368 (2020).
- [36] A. Eickbusch, V. Sivak, A. Z. Ding, S. S. Elder, S. R. Jha, J. Venkatraman, B. Royer, S. M. Girvin, R. J. Schoelkopf, and M. H. Devoret, Fast universal control of an oscillator with weak dispersive coupling to a qubit, *Nature Physics* **18**, 1464 (2022).
- [37] N. Ofek, A. Petrenko, R. Heeres, P. Reinhold, Z. Leghtas, B. Vlastakis, Y. Liu, L. Frunzio, S. Girvin, L. Jiang, *et al.*, Extending the lifetime of a quantum bit with error correction in superconducting circuits, *Nature* **536**, 441 (2016).
- [38] R. W. Heeres, P. Reinhold, N. Ofek, L. Frunzio, L. Jiang, M. H. Devoret, and R. J. Schoelkopf, Implementing a universal gate set on a logical qubit encoded in an oscillator, *Nature communications* **8**, 94 (2017).
- [39] L. Hu, Y. Ma, W. Cai, X. Mu, Y. Xu, W. Wang, Y. Wu, H. Wang, Y. Song, C.-L. Zou, *et al.*, Quantum error correction and universal gate set operation on a binomial bosonic logical qubit, *Nature Physics* **15**, 503 (2019).
- [40] R. W. Heeres, B. Vlastakis, E. Holland, S. Krastanov, V. V. Albert, L. Frunzio, L. Jiang, and R. J. Schoelkopf, Cavity state manipulation using photon-number selective phase gates, *Physical review letters* **115**, 137002 (2015).
- [41] D. Meekhof, C. Monroe, B. King, W. M. Itano, and D. J. Wineland, Generation of nonclassical motional states of a trapped atom, *Physical review letters* **76**, 1796 (1996).
- [42] B. Hacker, S. Welte, S. Daiss, A. Shaukat, S. Ritter, L. Li, and G. Rempe, Deterministic creation of entangled atom–light schrödinger-cat states, *Nature Photonics* **13**, 110 (2019).
- [43] E. A. Wollack, A. Y. Cleland, R. G. Gruenke, Z. Wang, P. Arrangoiz-Arriola, and A. H. Safavi-Naeini, Quantum state preparation and tomography of entangled mechanical resonators, *Nature* **604**, 463 (2022).
- [44] X. Pan, J. Schwinger, N.-N. Huang, P. Song, W. Chua, F. Hanamura, A. Joshi, F. Valadares, R. Filip, and Y. Y. Gao, Protecting the quantum interference of cat states by phase-space compression, *Physical Review X* **13**, 021004 (2023).
- [45] S. Colombo, E. Pedrozo-Peñañiel, A. F. Adiyatullin, Z. Li, E. Mendez, C. Shu, and V. Vuletić, Time-reversal-based quantum metrology with many-body entangled states, *Nature Physics* **18**, 925 (2022).
- [46] A. Blais, A. L. Grimsmo, S. M. Girvin, and A. Wallraff, Circuit quantum electrodynamics, *Reviews of Modern Physics* **93**, 025005 (2021).

Supplementary Information

I. OPTIMALITY OF THE PROTOCOL

The protocol consists of three parts: state preparation, estimated process and projection measurement as shown in the main text, in which state-transfer unitaries $\hat{O}_{1,2}$ can be done with any unitary for which the following holds:

$$\begin{aligned} |g\psi\rangle &= \hat{O}_1|g0\rangle, \\ |g0\rangle &= \hat{O}_2|g\psi\rangle. \end{aligned} \quad (2)$$

Note that the second line is equivalent to $\hat{O}_2^\dagger|g0\rangle = |g\psi\rangle$ and $\langle g0|\hat{O}_2 = \langle g\psi|$. Let us denote the final state before the qubit-cavity measurements as $|\psi_{\text{final}}\rangle = \hat{O}_2\hat{U}(\beta)\hat{O}_1|g0\rangle$ and the state with encoded parameter as $|g\psi(\beta)\rangle = \hat{U}(\beta)\hat{O}_1|g0\rangle$. The probability after the qubit-cavity measurements, i.e., projection into $|g0\rangle$ can be expressed as

$$\begin{aligned} p_{g0} &= \langle g0|\psi_{\text{final}}\rangle\langle\psi_{\text{final}}|g0\rangle \\ &= \langle g0|\hat{O}_2\hat{U}(\beta)\hat{O}_1|g0\rangle\langle g0|\hat{O}_1^\dagger\hat{U}^\dagger(\beta)\hat{O}_2^\dagger|g0\rangle \\ &= \langle g0|\hat{O}_2|g\psi(\beta)\rangle\langle g\psi(\beta)|\hat{O}_2^\dagger|g0\rangle \\ &= \langle g\psi|g\psi(\beta)\rangle\langle g\psi(\beta)|g\psi\rangle \\ &= |\langle\psi|\psi(\beta)\rangle|^2 \end{aligned} \quad (3)$$

This overlap probability contains information regarding the parameter β and is achieved with two state-transfer unitaries and standard qubit-cavity measurements.

To assess the sensitivity of the probability for parameter estimation, we compute the FI [34] for binary outcome:

$$\text{FI} = \frac{1}{p_{g0}(1-p_{g0})} \left(\frac{\partial p_{g0}}{\partial \beta} \right)^2. \quad (4)$$

The FI depends on particular measurement setting. An optimal measurement setting allows the FI to reach the QFI $4(\Delta\hat{B})^2$, which now only depends on the state and encoding operator of the corresponding parameter of interest. We now show that our measurement setting is optimal, i.e., the FI saturates the QFI when $\beta \rightarrow 0$. In this case, we write $\hat{U}(\beta) = e^{i\hat{B}\beta} \approx \mathbb{1} + i\hat{B}\beta - \hat{B}^2\beta^2/2 - i\hat{B}^3\beta^3/6 + \hat{B}^4\beta^4/24$ such that the probability reads

$$\begin{aligned} p_{g0} &= |\langle\psi|\hat{U}(\beta)|\psi\rangle|^2 \\ &\approx 1 - \beta^2(\Delta\hat{B})^2 \\ &\quad + \beta^4 \left(\frac{1}{12}\langle\hat{B}^4\rangle - \frac{1}{3}\langle\hat{B}\rangle\langle\hat{B}^3\rangle + \frac{1}{4}\langle\hat{B}^2\rangle^2 \right) \end{aligned} \quad (5)$$

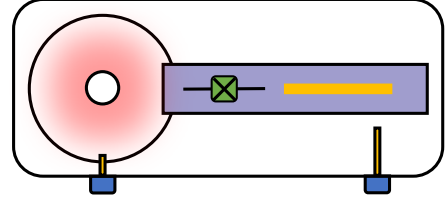


FIG. 5. **Schematic representation of 3D cQED hardware.** The device comprises three essential components: the cavity functions as the bosonic mode, the transmon introduces nonlinearity, and the resonator serves for signal readout. Additionally, one pin is coupled with the cavity for driving, while the transmon and resonator share the same channel for operation.

Referring to Eq. (4), the FI can be written as

$$\begin{aligned} \text{FI} &= \frac{1}{p_{g0}(1-p_{g0})} \left(\frac{\partial p_{g0}}{\partial \beta} \right)^2 \\ &\approx 4(\Delta\hat{B})^2 \\ &\quad - \beta^2 \left(\langle\hat{B}^4\rangle - 4\langle\hat{B}\rangle\langle\hat{B}^3\rangle + 3\langle\hat{B}^2\rangle^2 - 4(\Delta\hat{B})^2 \right) \end{aligned} \quad (6)$$

where the absolute term independent of β represents QFI.

II. DEVICE AND SYSTEM PARAMETERS

Our device consists of a standard three-dimensional (3D) cavity, an ancillary transmon and a planar readout resonator, see Fig. 5. The cavity is made of high-purity (4N) aluminum and is a $\lambda/4$ cylinder-shaped transmission line surrounded by a wall. The readout resonator is deposited together with the transmon on the sapphire using double-angle evaporation technique. The sapphire is inserted in the tunnel, with the pad slightly extending to the cavity. The cavity serves as a high-Q quantum memory to store a bosonic mode and is designed to dispersively couple with the ancillary transmon qubit, which provides the necessary nonlinearity. The low-Q readout resonator is also dispersively coupled with the transmon qubit, enabling fast single-shot measurement. The Hamiltonian of the system can be written as:

$$\hat{H} = \hat{H}_0 + \hat{H}_d, \quad (7)$$

where \hat{H}_0 (\hat{H}_d) incorporates the bare (drive) terms

$$H_0 = \Delta\hat{a}^\dagger\hat{a} - \chi\hat{a}^\dagger\hat{a}\hat{q}^\dagger\hat{q} - \frac{\alpha}{2}\hat{q}^\dagger\hat{q}^\dagger\hat{q}\hat{q} - \frac{K}{2}\hat{a}^\dagger\hat{a}^\dagger\hat{a}\hat{a} - \frac{\chi'}{2}\hat{q}^\dagger\hat{q}\hat{a}^\dagger\hat{a}\hat{a}$$

$$\hat{H}_d = i\zeta(t)\hat{a}^\dagger - i\zeta(t)^*\hat{a} + i\epsilon(t)\hat{q}^\dagger - i\epsilon(t)^*\hat{q}.$$

Here \hat{a} (\hat{q}) denotes the annihilation operator of the cavity (transmon), Δ the frequency detuning between cavity and its drive, χ the dispersive coupling, χ' the second

order dispersive coupling, α the transmon anharmonicity, K cavity anharmonicity or Kerr, ζ and ϵ respectively the drive strength of the cavity and transmon.

The system parameters are summarized in Table I.

Cavity frequency (GHz)	$\omega_c/2\pi$	4.587
Qubit frequency (GHz)	$\omega_q/2\pi$	5.277
Resonator frequency (GHz)	$\omega_r/2\pi$	7.617
Cavity single-photon lifetime (ms)	$T_{c,1}$	1
Transmon energy lifetime (μ s)	$T_{q,1}$	96
Transmon coherence lifetime (μ s)	$T_{q,2}$	15.47
Cavity anharmonicity (kHz)	$K/2\pi$	6
Transmon anharmonicity (kHz)	$\alpha/2\pi$	175.3
1st cavity-transmon dispersive shift (MHz)	$\chi/2\pi$	1.423
2nd cavity-transmon dispersive shift (MHz)	$\chi'/2\pi$	15.76
Transmon-resonator dispersive shift (MHz)	$\chi_{qt}/2\pi$	0.64

TABLE I. **System parameters.** Summary of the key system parameters and lifetimes.

Note that for sufficiently high transmon anharmonicity, it can be effectively treated as a qubit (two-level system with $|g\rangle$ ($|e\rangle$) as the ground (excited) level). The first two terms in the bare Hamiltonian then becomes $\Delta\hat{a}^\dagger\hat{a} - \chi\hat{a}^\dagger\hat{a}|e\rangle\langle e|$, which reduces to $(\chi/2)\hat{\sigma}_z\hat{a}^\dagger\hat{a}$ for $\Delta = \chi/2$ that is chosen.

III. PRELIMINARY INVESTIGATIONS USING DIFFERENT STATES

Useful states for achieving low estimation error $\Delta\beta$ encoded with an operator \hat{B} via $\hat{U}(\beta) = e^{i\hat{B}\beta}$ are those with high variance $(\Delta\hat{B})^2$.

In the context of phase estimation, we investigate several states such as CS $|\alpha\rangle$, superposition of Fock states $(|0\rangle + |N\rangle)/\sqrt{2}$, squeezed vacuum $e^{\frac{-r}{2}(\hat{a}\hat{a} - \hat{a}^\dagger\hat{a}^\dagger)}|0\rangle$, and SCS $\mathcal{N}(|0\rangle + |\alpha\rangle)$. Here, the normalisation factor $\mathcal{N}_\alpha = 1/\sqrt{2(1 + e^{-|\alpha|^2/2})}$. The average photon number $\bar{n} = \langle\hat{a}^\dagger\hat{a}\rangle$ of these states are respectively $|\alpha|^2$, $N/2$, $\sinh^2 r$, and $\mathcal{N}_\alpha^2|\alpha|^2$. The QFI $4(\Delta\hat{n})^2$ of these states in terms of n are respectively $4\bar{n}$, $4\bar{n}^2$, $8\bar{n}^2 + 8\bar{n}$, and $4((1 - \mathcal{N}_\alpha^2)/\mathcal{N}_\alpha^2)\bar{n}^2 + 4\bar{n}$. The QFI of SCS reduces to $4\bar{n}^2 + 4\bar{n}$ for large \bar{n} as $\mathcal{N}_\alpha \approx 1/\sqrt{2}$.

Experimentally, we realise these states and compute the corresponding FI with the same method as described in the main text, see Fig. 6(a). The comparison is made for states with the same photon number $\bar{n} = 0.5$. It is apparent that the SCS offers the highest FI. Although squeezed vacuum is supposed to give a higher theoretical QFI, the state is harder to generate as it requires high squeezing. Highly squeezed states exhibit increased spreading in phase space, making them susceptible to the Kerr effect, which, in turn, hinders quantum-enhanced sensitivity. A viable strategy to mitigate the impact of the Kerr effect involves minimizing the coupling between the cavity and transmon. By reducing this coupling, the undesirable consequences of the Kerr effect can be alleviated, contributing to enhanced quantum sensitivity.

Therefore, we discern that with our device, the optimal states are SCS.

Similarly, in the context of amplitude estimation the QFI $4(\Delta\hat{x})^2$ for CS, squeezed vacuum, and SCS are respectively given by 4, $8\sqrt{\bar{n}(\bar{n} + 1)} + 8\bar{n} + 4$, and $8\bar{n} + 4$. The QFI for superposition of Fock states is 4, $12 + 4\sqrt{2}$, and $8\bar{n} + 4$ for $\bar{n} = 0.5$, $\bar{n} = 1$, and $\bar{n} > 1$ respectively.

We experimentally perform the protocol and compute the FI, see Fig. 6(b). Here, unlike the phase estimation, the highest FI is achieved by squeezed vacuum followed by SCS. However, squeezed vacuum with higher n is less robust to Kerr and harder to realise. Therefore, we proceed with SCS for more detailed analysis.

The phase and amplitude estimation underscore the importance of selecting appropriate quantum states to achieve the best precision. Accompanied with practical considerations, this presents an optimal quantum metrology.

IV. IMPERFECTION OF THE SYSTEM

In the experiment, we use gradient ascent pulse engineering (GRAPE) pulse to realize the two state transfer of the protocol. The GRAPE pulses ($\zeta(t)$ and $\epsilon(t)$) are optimized in an ideal system without imperfections. In practice, each element of the system is susceptible to environmental noise, making it crucial to account for the coherence and energy decay rate of both the cavity and transmon qubit. Table I presents the corresponding parameters. To account for decoherence, the simulations in the main text (all the sequence) are performed with the following master equation:

$$\frac{d\rho}{dt} = -\frac{i}{\hbar}[\hat{H}, \rho] + \sum_k \hat{L}_k \rho \hat{L}_k^\dagger - \frac{1}{2}(\hat{L}_k^\dagger \hat{L}_k \rho + \rho \hat{L}_k^\dagger \hat{L}_k), \quad (8)$$

where \hat{L}_k denotes the jump operator for the corresponding decoherence. We consider five types of decoherence: qubit relaxation $\hat{L}_1 = \hat{q}(1 + E_q)/\sqrt{T_{q,1}}$, qubit thermal excitation $\hat{L}_2 = \hat{q}^\dagger E_q/\sqrt{T_{q,1}}$, qubit dephasing $\hat{L}_3 = \hat{q}^\dagger \hat{q}/\sqrt{T_{q,2}}$, cavity relaxation $\hat{L}_4 = \hat{a}(1 + E_c)/\sqrt{T_{c,1}}$, cavity thermal excitation $\hat{L}_5 = \hat{a}^\dagger E_c/\sqrt{T_{c,1}}$, where E_c, E_q are the spontaneous excitation rate of the cavity and qubit population respectively.

V. COMPREHENSIVE ANALYSIS FOR PARAMETER ESTIMATION

In this section we provide analysis on the practical position of maximum sensitivity, further details on amplitude estimation, and metrological gain vs measurement repetitions.

In part I, we see that ideally maximum FI is achieved at $\beta \rightarrow 0$. In the presence of imperfections, this is not

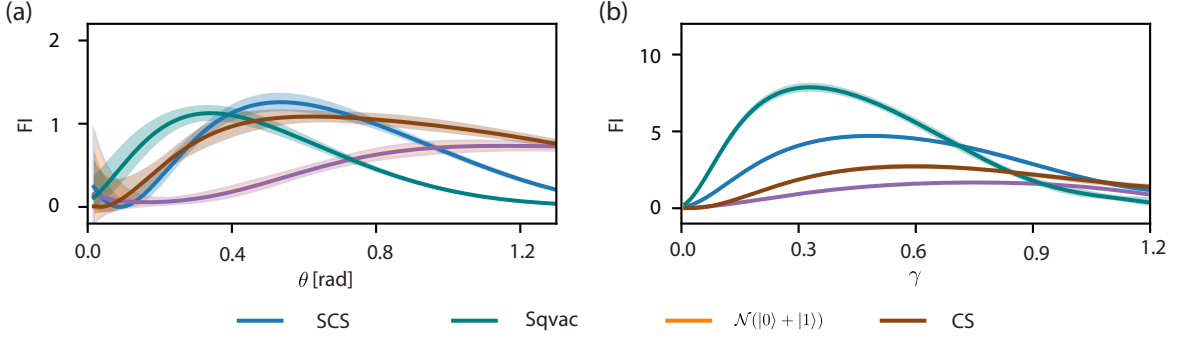


FIG. 6. **Phase and amplitude estimation utilizing various states.** The FI of phase estimation (a) and amplitude estimation (b) utilizing CS, superposition of Fock states, squeezed vacuum (Sqvac) and SCS with fixed average photon number $n = 0.5$.

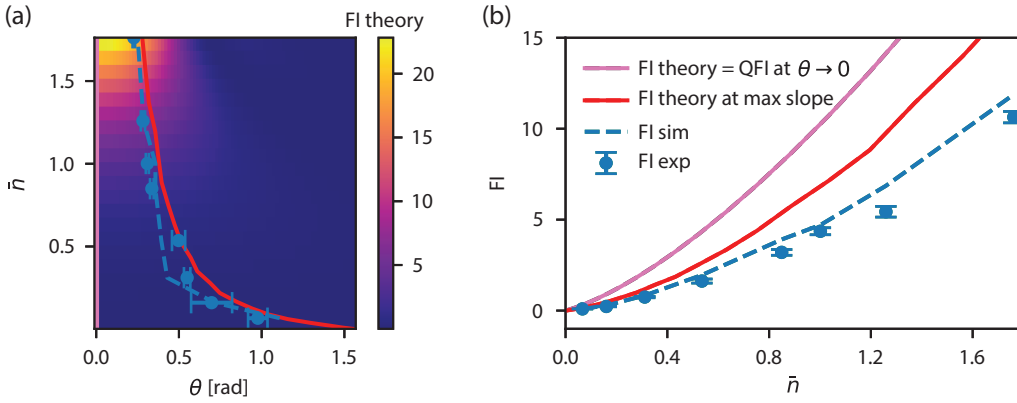


FIG. 7. **Position of maximum sensitivity.** (a) Theoretical FI for SCS vs θ for states with different average photon number \bar{n} . The pink and red lines are FI at $\beta \rightarrow 0$ and maximum probability slope $|\partial p/\partial \theta|$ respectively. Experimental data (blue dot) and simulation (blue dash line) from Fig. 3(a) in the main text are replotted here for comparison. (b) The corresponding different FI are plotted for comparison.

the case. To exemplify this let us first compute the FI of SCS for phase estimation. The probability of overlap is given by

$$p = \frac{|\langle \psi | \psi(\theta) \rangle|^2}{4(1 + e^{-\frac{\alpha^2}{2}})} |1 + 2e^{-\frac{\alpha^2}{2}} + e^{-\alpha^2(1 - e^{i\theta})}|^2. \quad (9)$$

From p , the theoretical FI can be derived analytically. This FI is plotted in Fig. 7(a) vs θ for SCS with different average photon number \bar{n} . We note that at $\beta \rightarrow 0$ (pink line), the FI saturates the QFI. We also plotted the FI at the maximum slope $|\partial p/\partial \theta|$ as red line. We note that the experimental data (blue circles) follows this path closely. This supports a strategy that the practical position of maximum sensitivity is around the maximum slope of probability. The comparison of the corresponding FI is plotted in Fig. 7(b).

The supplemental analysis of amplitude estimation is shown in Fig. 8. Similar to phase estimation, it is essential to gain insights into the mean sensitivity above

maximum FI of CS and the γ offset at which the FI is optimal. With the increase of photon number, the average FI increases linearly while the optimal amplitude sensor point is moving to 0 as shown in Fig. 8(a). The optimal amplitude sensor point can also be shifted to 0 by adding a displacement to the initial state in the GRAPE pulse, which is crucial for direct amplitude sensing. Furthermore, to estimate the amplitude estimation error directly via $\Delta\gamma = \Delta p/|\partial p/\partial \gamma|$, we present a benchmark in Fig. 3(c). The amplitude estimation error for the CS remains constant even with an increase in the average photon number. In contrast, the estimation error using SCS exhibits an almost linear relationship with the average photon number and shows an optimal gain of 9.3(5)dB compared to the CS.

Furthermore, we also perform amplitude estimation with unbalanced SCS for optimization. We note two distinct scenarios: one with a fixed average photon number of 1 and another with a fixed $\alpha = 1.6$, shown in Fig. 9(a) and Fig. 9(b), respectively. The former shows the less weight on the α component of SCS yields a higher sensi-

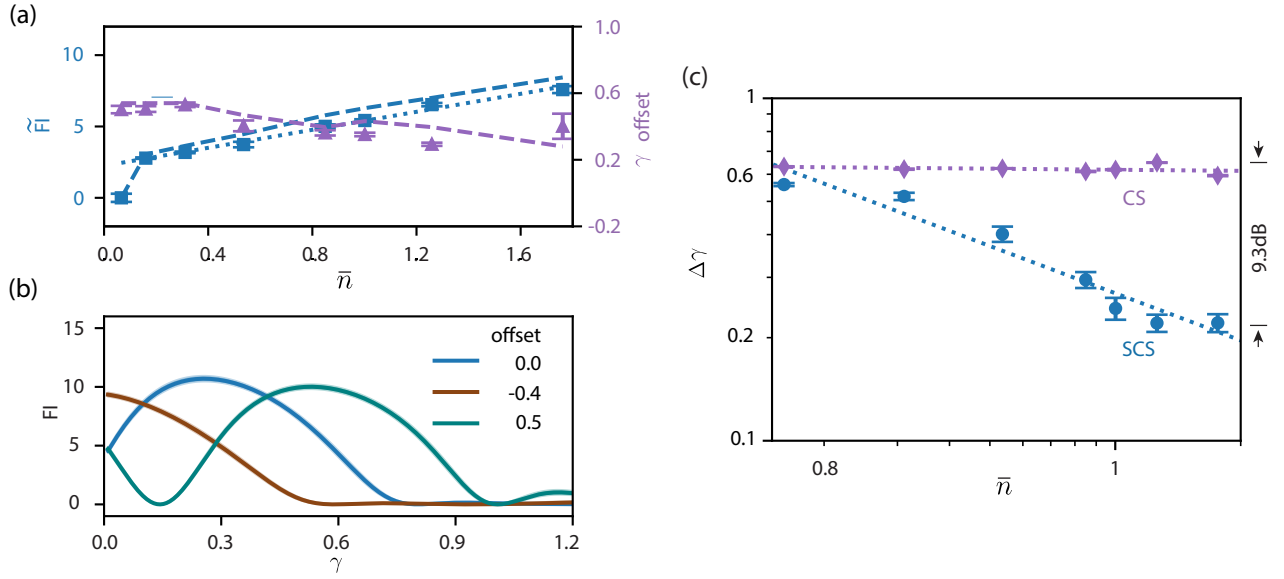


FIG. 8. **Performance of quantum-enhanced amplitude precision.** (a) The average FI of SCS for which it is above the max FI of CS and γ offset at which FI is maximum vs n . The dotted line is linear fit of $3.2(2)\bar{n}^{1.0(3)} + 2.2(1)$. (b) The same protocol as in Fig. 4(c) in main text with initial states prepared with an offset. (c) The amplitude precision vs n for both SCS (blue circles) and CS (purple diamonds). The dotted lines are linear fit of $\log(\Delta\gamma) = a \log(\Delta n) + b$ with a and b as free parameters. The fitted parameters are $a, b = -0.460(3), -1.311(2)$ for SCS and $a, b = -0.0105(2), -0.480(1)$ for CS.

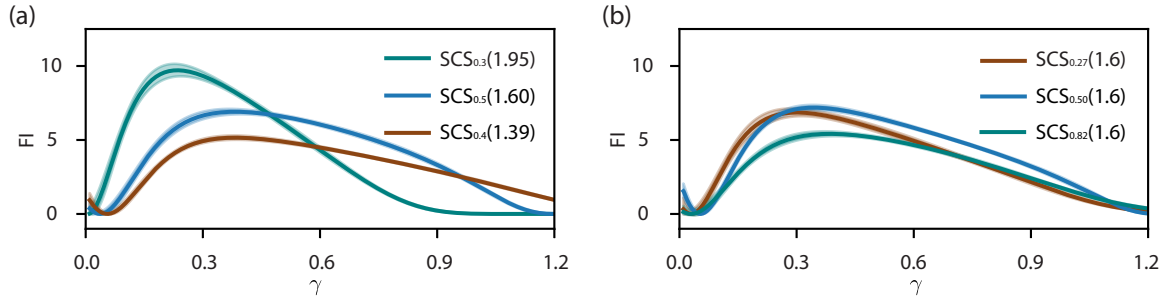


FIG. 9. **Demonstration of amplitude estimation by state optimization.** The FI of SCS of different weights with (a) fixed photon number $n = 1$ and (b) fixed $\alpha = 1.6$. The corresponding shaded area indicates standard deviation from bootstrap.

tivity. In the latter, the optimal sensitivity with limited α is achieved by utilizing balanced components. Finally, an important factor to consider for sensing applications is the measurement repetitions, which also directly translates to the total duration of the protocol. The highest metrological gain for phase and amplitude estimation we report in the main text was done with 1000 measurement

repetitions. The respective gain vs measurement repetitions are plotted in Fig. 10. Notably, the gain for both phase and amplitude estimation stabilizes at ~ 600 measurement repetitions. It shows that beyond this point, the single shot measurements is enough to provide meaningful statistics.

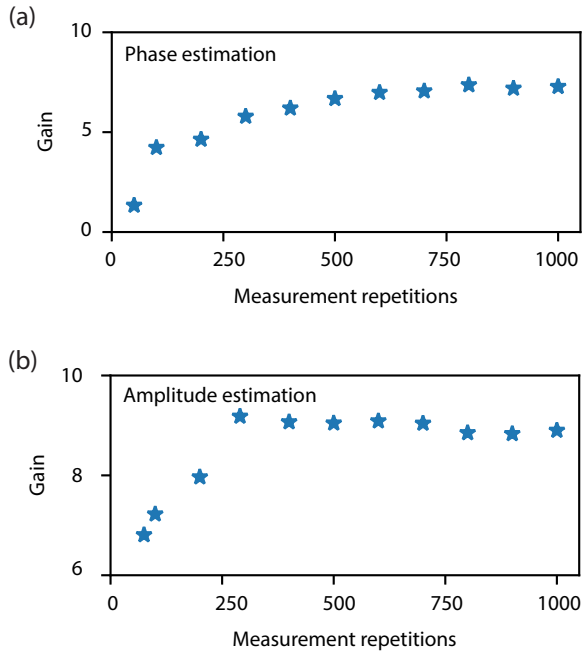


FIG. 10. **Metrological gain vs measurement repetitions.** The gain of SCS over CS for: (a) phase estimation and (b) amplitude estimation for different measurement repetitions.